Optical-resolution photoacoustic microscopy with a needle-shaped beam

Rui Cao[1#], Jingjing Zhao[2#], Lei Li[1], Lin Du[3], Yide Zhang[1], Yilin Luo[1], Laiming Jiang[4], Samuel Davis[1], Qifa Zhou[4], Adam de la Zerda[2,5,6*], Lihong V Wang[1*]

[1]Caltech Optical Imaging Laboratory, Andrew and Peggy Cherng Department of Medical Engineering, Department of Electrical Engineering, California Institute of Technology, Pasadena, California, USA

[2]Department of Structural Biology, Stanford University School of Medicine, Stanford University, Stanford, California, USA

[3]Department of Electrical and Systems Engineering, University of Pennsylvania, Philadelphia, Pennsylvania, USA

[4]Department of Biomedical Engineering and Ophthalmology, Viterbi School of Engineering, University of Southern California, Los Angeles, California, USA

[5]Biophysics Program, Molecular Imaging Program, and Bio-X Program at Stanford University, Stanford, California, USA

[6]Chan Zuckerberg Biohub, San Francisco, California, USA

[#]These authors contributed equally: Rui Cao and Jingjing Zhao

*Correspondence: adlz@stanford.edu; LVW@caltech.edu

Abstract

Optical-resolution photoacoustic microscopy (OR-PAM) can visualize wavelength-dependent optical absorption at the cellular level. However, OR-PAM suffers from a limited depth of field (DOF) due to the tight

focus of the optical excitation beam, making it challenging to acquire high-resolution images of samples with uneven surfaces or high-quality volumetric images without z-scanning. To overcome this limitation, we propose needle-shaped beam photoacoustic microscopy (NB-PAM), which can extend the DOF to up to ~28-fold Rayleigh lengths via customized diffractive optical elements (DOEs). The DOE generate a needle beam with a well-maintained beam diameter, a uniform axial intensity distribution, and negligible sidelobes. The advantage of using NB-PAM is demonstrated by both histology-like imaging of fresh slide-free organs using a 266 nm laser and in vivo mouse brain vasculature imaging using a 532 nm laser. The approach provides new perspectives for slide-free intraoperative pathological imaging and *in-vivo* organ-level imaging.

In past decades, rapid developments in optical imaging technologies have revolutionized life science. For high-resolution optical imaging, a tight optical focus is usually needed to achieve the diffraction-limited resolution in optical microscopy, resulting in a limited depth of field (DOF). The narrow DOF causes the degradation of lateral resolution at a distance away from the optical focal plane. It hinders fast high-resolution imaging of slide-free specimens with irregular surfaces or 3D volumetric imaging of organs, which usually requires time-consuming axial scanning at multiple planes and complicated image processing. For time-sensitive imaging applications like intraoperative histology or cerebral hemodynamics, the capability of direct imaging irregular surfaces with a large DOF at high resolution is desired. However, a large DOF with a tight optical focus for high-resolution imaging is not easily achievable.

To address the need for an extended DOF in high-resolution microscopes, researchers have explored different approaches. The extended DOF can be achieved via dynamic remote focusing or decoupled illumination and detection (e.g., light-sheet microscope)[1–6]. Nonetheless, it requires complicated geometry and significantly increases the system complexity and cost. Alternatively, multi-plane microscopes have been implemented through spatial and spectral multiplexing techniques[7–10]. However, the 3D multi-plane imaging is susceptible to misalignment of the detection channels and demands accurate calibration of the image planes prior to imaging. Fourier ptychographic microscopy (FPM) used a simple configuration and adopted the wavefront correction strategy to extend the DOF computationally[11]. But the image reconstruction algorithm for FPM assumes a thin sample target transilluminated with oblique plane waves, limiting its applications for imaging thick specimens or organs *in vivo*. In addition, many researchers have applied non-diffracting beams (e.g., Bessel beam and Airy beam) for extended DOFs in microscopy[12–18]. However, the image quality usually suffered from severe sidelobes and low efficiency[19]. Recently, deep learning techniques have been applied to improve the DOF[20–22]. But intensive training with lots of ground-truth data is needed, which may not be easy to acquire for specific subjects.

As an emerging technology, photoacoustic microscopy (PAM) can directly image the distribution of intrinsic or extrinsic optical absorbers by detecting optical absorption-induced acoustic signals[23,24]. Benefitting from rich intrinsic contrasts in biological tissues, label-free PAM has been demonstrated in imaging various biological components, such as DNA/RNA[25–27], cytochrome[28], hemoglobin[29–31], melanoma[32], and lipid[33,34]. Different than other pure optical imaging techniques, 3D volumetric photoacoustic (PA) images can be directly reconstructed with only 2D scanning utilizing the time-of-flight information carried by PA signals[23]. For high-resolution imaging, optical-resolution photoacoustic microscopy (OR-PAM) with a tight optical focus has been implemented[35,36]. However, OR-PAM still suffers from the trade-off between DOF and spatial resolution as other optical microscopy techniques—a higher spatial resolution corresponds to a narrower DOF, which compromises the image quality due to out-of-focus blurring in volumetric imaging or uneven surface imaging. Many efforts have been made in PAM to extend the DOF, such as utilizing Bessel beam[37–40], dynamic focusing[41–43], synthetic aperture focusing technique[44–46], and structured illumination[47,48]. But they suffer from strong sidelobes, slowdown of imaging, or complicated post-processing procedures.

To fill this gap, we present the optical-resolution needle-shaped beam photoacoustic microscopy (NB-PAM) with an extended DOF via customized diffractive optical elements (DOEs). The needle-shaped beam (NB) generated by the DOE is shown to have a DOF up to 28-fold Rayleigh lengths, while maintaining a relatively constant beam diameter, a uniform axial intensity distribution, and negligible sidelobes. As a thin glass plate, the DOE can be easily integrated into an existing optical system without rebuilding the optical setup (e.g., place it in front of the objective lens). We have demonstrated the NB-PAM with an extended DOF for irregular surface imaging and volumetric imaging without z-scanning. The histology-like PA imaging of fresh and slide-free organs was achieved using ultraviolet NB-PAM (UV-NB-PAM) at 266 nm, while the *in vivo* mouse brain vasculature images were acquired by visible NB-PAM (VIS-NB-PAM) at 532 nm.

Results:

The principle of NB-PAM via DOE

To form the NB, we developed DOEs to generate numerous closely adjacent foci along the axial direction (Fig. 1a-b). The beam length can be flexibly adjusted by increasing or decreasing the number of foci. The DOE phase is formulated as $P_{DOE}(x,y) = \sum_{m=1}^{M}\{[-\pi \cdot n \cdot (x^2+y^2) \cdot (1/f_m - 1/f)/\lambda - \pi \cdot m \cdot Ap] \cdot Loc_m(x,y)\}$, where (x,y) is the planar coordinate, λ is the light wavelength, f is the objective focal length in the medium, f_m is the destinated focal position, n is the refractive index of the surrounding medium, M is the foci number, m is the focus index, $Loc_m(x,y)$ is a binary matrix to allocate DOE pixels, Ap is a coefficient, $\pi \cdot m \cdot Ap$ is the phase regulator responsible for adjusting the beam diameter, and the item $[-\pi \cdot n \cdot (x^2+y^2) \cdot (1/f_m - 1/f)/\lambda - \pi \cdot m \cdot Ap]$ aims to shift the focus from f to f_m (Supplementary Fig. 1). The DOE pixels are equally and randomly allocated into m subsets (Fig. 1a), each of which belongs to one specific focus: e.g., for the pixel (x,y) allocated to f_1, $Loc_1(x,y) = 1$ and $Loc_{m\neq 1}(x,y) = 0$. The beam length is determined by $(f_m - f_1)$. The rule for determining the number of foci M is to control the average interval between two neighboring foci with no more than one Rayleigh length. We set f_1 to be coincident with the objective lens focus f. Therefore, the NB can be generated by using a customized DOE with the corresponding objective lens, as shown in Fig. 1b. The DOE was fabricated on a 500 μm thick fused silica substrate (Supplementary Fig. 2a), which has rectangular pixels with an alignment error of around one μm for the four-times lithography to achieve 16 heights (Supplementary Fig. 2b). More fabrication characterization can be found in Supplementary Fig. 2c-f and Supplementary Table 1.

We designed two DOEs for the UV-NB-PAM (266 nm) and VIS-NB-PAM (532 nm). The phase patterns for these two fabricated DOEs can be found in Supplementary Fig. 3a-b. The DOEs contain 1024×1024 pixels with

a feature size of 10 or 15 μm, depending on the input beam diameter. NBs with variable parameters can be generated using different DOEs and laser wavelengths. The DOE for 266 nm light was designed to generate 200 μm×1.2 μm NB (full-width-at-half-max beam length×minimal beam diameter), while the DOE for 532 nm light was designed to generate 1000 μm×2.3 μm NB. They were formed by 64 foci and 81 foci, respectively. The phase regulators were chosen as $0.022\pi \times m$ and $0.088\pi \times m$, where m is the focus index. The foci locations of each NB were optimized for a uniform axial intensity, as listed in Supplementary Fig. 3c-d. For the Gaussian beam with a focal spot size of 2.3 μm at 532 nm, the DOF is about 70 μm (two Rayleigh lengths), while the beam spot size will expand to ~31 μm at the distance of $\pm$500 μm. In comparison, the 1000 μm×2.3 μm NB maintains its diameter between ~2.3 μm (at the two ends) and ~2.7 μm (at the middle of the beam) over the entire 1000 μm depth range (~28-fold Rayleigh lengths) with relatively uniform axial intensity (Supplementary Fig. 4). In addition, we compared beam profiles of the Gaussian beam (focus diameter of 1.2 μm) and DOE-based NB (200 μm×1.2 μm) at 266 nm predicted via Fourier transform, showing NB can maintain the beam spot size much better along the z-axis than the Gaussian beam at same beam diameter (Fig. 1c-d). Please note that the NB has the smallest beam diameter at the two ends and a slightly larger beam diameter at the middle of the beam, which is different than the focused Gaussian beam with the smallest spot size at the focal plane.

To transform the conventional reflection-mode Gaussian beam OR-PAM into NB-PAM, we placed the DOE in the beam path before the objective lens (Fig. 1e). Through a customized objective lens consisting of an achromatic doublet and a correction lens, the phase-modulated beam was converted to NB around the original focal plane of the Gaussian beam. Using DOEs, we achieved an efficiency of up to 30% input beam energy. Compared to a Bessel beam with a sidelobe to main lobe ratio up to 20%, NB can be optimized to have negligible sidelobes, avoiding the need for complicated image processing in NB-PAM. In contrast to optical resolution Gaussian beam photoacoustic microscopy (GB-PAM), the NB-PAM allows better 2D images of irregular

surfaces or volumetric imaging of thick specimens, as shown in the simulation results (Fig. 1f-g).

NB-PAM system performance

The resolution and DOF of NB-PAM systems were measured and compared with conventional GB-PAM. A positive 1951 USAF resolution test target was imaged at wavelengths of 266 nm and 532 nm using both GB-PAM and NB-PAM. Images of the resolution target by ultraviolet GB-PAM (UV-GB-PAM) and UV-NB-PAM were acquired at different axial locations (Fig. 2a), which clearly demonstrates the improved DOF. The UV-GB-PAM has an effective NA of 0.16, while the UV-NB-PAM used the DOE for 200 μm×1.2 μm NB. Please note that the DOF can be slightly larger than 200 μm since we defined the NB length by using the middle part. The simulation results of beam diameter and intensity along axial positions were calculated for both 1.2 μm GB and 200 μm×1.2 μm NB (Supplementary Fig. 5). The close-up images by both UV-GB-PAM and UV-NB-PAM (Fig. 2b and Fig. 2d) show good image quality and a well-resolved pattern at the focal plane (z = 0 μm). In contrast, the UV-GB-PAM generated a blurred image at a depth of 105 μm (Fig. 2c), while the UV-NB-PAM still maintained the image quality (Fig. 2e). Profiles of element 6 from group 7 measured by both UV-GB-PAM and UV-NB-PAM at z = 0 μm are shown in Fig. 2f. Lateral resolutions were measured by imaging a sharp edge and quantified by edge spread functions and derived line spread functions (Fig. 2g). The conventional UV-GB-PAM has a full-width at half-maximum (FWHM) resolution of 1.1 μm at 266 nm, corresponding to a DOF of ~30 μm. The measured FWHM resolution of UV-NB-PAM is about 1.2 μm, well-matched with the theoretical calculations. Similarly, we imaged the resolution target using VIS-GB-PAM and VIS-NB-PAM with 1000 μm×2.3 μm NB (Supplementary Fig. 6).

The 3D volumetric imaging capabilities of UV-NB-PAM with 200 μm×1.2 μm NB and VIS-NB-PAM with 1000 μm×2.3 μm NB were compared with conventional UV-GB-PAM and VIS-GB-PAM of 0.16 NA through imaging carbon particles and fibers randomly distributed in a thick agarose block. The XY-maximal amplitude

projection (MAP) image of particles over the depth of ~400 μm acquired by UV-NB-PAM (Fig. 3a) shows more uniform particle sizes and clearer images in comparison to the MAP image acquired by UV-GB-PAM (Fig. 3b), benefitting from the improved DOF. Another evidence of the improved image quality can be found from the YZ MAP images of a small fraction of phantom (Supplementary Fig. 7). The YZ-projection image by UV-NB-PAM shows well-maintained particle sizes at different depths, while the UV-GB-PAM showed noticeable blurring in out-of-focus particles due to the limited DOF. It is worth mentioning that the confocally aligned ultrasonic transducer also have a limited DOF (Supplementary Fig. 8), which affected the detection sensitivity of photoacoustic signals at different depths. To compensate for the sensitivity difference along Z-axis, we implemented the time-dependent gain compensation in photoacoustic signals after differentiating photoacoustic signals and background noise by a threshold of 3 times standard deviation of background noise. With the time-dependent gain compensation, the acoustic signal difference at different depth due to the limited acoustical DOF was alleviated. By applying virtual sectioning with the aid of time-of-flight information, we can isolate the particles at different depths with a step size of the acoustical resolution (i.e., ~30 μm), determined by the ultrasonic transducer bandwidth. In the sectioned UV-GB-PAM images, it is clear that the particles distributed at a distance (i.e., $z = 90\ \mu m$) from the focal plane (i.e., $z = 0\ \mu m$) is severely blurred and distorted, while the UV-NB-PAM images show improved image quality (Fig. 3c).

In addition, we acquired the depth-encoded MAP images of carbon fibers randomly distributed within an agarose phantom using both conventional VIS-GB-PAM (Fig. 4a) and VIS-NB-PAM with 1000 μm×2.3 μm NB (Fig. 4b). Depth information is encoded in different colors, ranging from 0 mm to 1.15 mm. The close-up images show that the VIS-GB-PAM cannot image fibers at a distance from the focal plane in high-resolution and high sensitivity. (Fig. 4c-f). In contrast, VIS-NB-PAM images (Fig. 4c-f) shows more fibers without blurring within 1 mm depth. The optical focal plane is located at ~0.5 mm depth.

Slide-free histological imaging by UV-NB-PAM

Utilizing the strong absorption of ultraviolet light by DNA/RNA, label-free UV-GB-PAM has been demonstrated to acquire histology-like images without excessive sample preparation[25]. However, slide-free histology imaging usually faces the difficulty of imaging irregular surfaces in high resolution. To demonstrate the advantages of UV-NB-PAM for fast slide-free histology imaging, we compared the conventional UV-GB-PAM and UV-NB-PAM of slide-free fresh organs with irregular surfaces. The UV-GB-PAM of a mouse lung (Fig. 5a) showed blurred cell nuclei in the close-up images and missing features (yellow arrow in Fig. 5a), caused by the limited DOF and large height fluctuation in the organ surface. The small fraction of the brighter part in Fig. 5a indicates the areas around the optical focal plane of UV-GB-PAM, which have a better signal-to-noise ratio and a better resolution than out-of-focus areas. In contrast, the UV-NB-PAM of the lung (Fig. 5b) showed some well-resolved lung features which are not identifiable in the UV-GB-PAM image (indicated by the arrow). The close-up images in Fig. 5b show well-distinguished cell nuclei, while the corresponding area in the UV-GB-PAM is blurred. In addition, we imaged the unprocessed fresh mouse brain in top view by both UV-GB-PAM (Fig. 5c) and UV-NB-PAM (Fig. 5d). The comparison between close-up images acquired by conventional UV-GB-PAM (Fig. 5c) and UV-NB-PAM (Fig. 5d) clearly demonstrated the advantage of UV-NB-PAM for slide-free histological imaging, which usually requires a large DOF for unprocessed specimens with irregular surfaces. Please note that there was still some residual blood inside major cortical blood vessels, which also generated some photoacoustic signals. This can be easily avoided by saline perfusion before the brain harvesting. Additional images of a fresh mouse liver acquired by UV-NB-PAM and UV-GB-PAM can be found in Supplementary Fig. 9.

***In vivo* VIS-NB-PAM of mouse brain vasculature**

With the capability of imaging the oxyhemoglobin and deoxyhemoglobin in a label-free manner, the VIS-GB-

PAM has been widely used to image the brain vasculature and function. However, the large curvature of mouse brain cortex affected fast high-resolution imaging of the full cortical vessels. To demonstrate the advantages of VIS-NB-PAM for *in vivo* brain vasculature imaging, we imaged a mouse brain with an intact skull and a mouse with the skull removed via craniotomy surgery. For better visualization of the brain curvature, we encoded the depth into different colors. Although the conventional VIS-GB-PAM of the mouse brain without a skull shows small cortical vessels in detail, it missed many vessels at the edge areas (Fig. 6a). In contrast, the color-encoded VIS-NB-PAM clearly shows more vessels at the edge areas, even with a distance of 700-800 μm away from the top surface (Fig. 6b). The irregular nonvessel-shaped structures in Fig. 6a and Fig. 6b may be due to imperfect surgical procedures, which resulted in minor bleeding in the brain. The VIS-GB-PAM of a mouse brain with an intact skull shows fewer blood vessels (Fig. 6c) than the mouse brain without a skull, mostly due to the skull scattering and attenuation of light. Although the skull scattering also affects NB, the VIS-NB-PAM still shows more vessels and better image quality (Fig. 6d) than the conventional VIS-GB-PAM. Some edges areas with vessels are slightly blurred, which may be due to the skull's impact on light propagation. It took about 20 minutes to scan the brain vasculature with step sizes of 1.25 μm for the fast axis and 5 μm for the slow axis.

Discussion

In this work, we have designed high-efficiency DOEs to generate needle-shaped beams for both VIS-NB-PAM (532 nm) and UV-NB-PAM (266 nm) in reflection mode. It has an elongated DOF for high-resolution imaging, which is crucial for 2D imaging of uneven surfaces or 3D volumetric imaging. Utilizing the needle-shaped beam, we have demonstrated ~6 times DOF improvement in UV-NB-PAM and ~14 times DOF improvement in VIS-NB-PAM. Please note the current DOF improvements are not the theoretical limit, which can be further adjusted according to the laser energy and required efficiency for PAM. Using the UV-NB-PAM, slide-free histological imaging of fresh organs has been demonstrated, showing clear advantages compared to conventional UV-GB-

PAM systems. It addresses the critical challenge of high-resolution imaging of uneven surfaces in unprocessed slide-free specimens, allowing rapid intraoperative pathological diagnostics via photoacoustic histology. In addition, we demonstrated *in vivo* VIS-NB-PAM of mouse brain vessels with the improved FOV and DOF at the wavelength of 532 nm.

Our work brings new opportunities to not only PAM technologies but also other high-resolution microscopy technologies for biological and biomedical applications where a large DOF is needed. Supplementary Table S3 compares our NB-PAM and previously developed methods to extend DOFs in PAM (detailed discussion can be found in the supplementary note). The DOE-based NB can convert most of the current microscopy systems with minimal modifications for an extended DOF. The NB generated by phase-only modulation can be combined with other structure illuminations (e.g., multiple foci) and fast scanning approaches (e.g., galvo scanning) to further improve the imaging speed. It is worth noting that the imaging speed of our current PAM is still slow due to the limited motor scanning speed for VIS-PAM (i.e., <10 mm/s) and the relatively low laser repetition rate for UV-PAM (i.e., 10 kHz). Developments of fast OR-PAM with NB would exploit NB's advantage in time-sensitive applications. Compared to SLM, the DOEs have a much higher damage threshold which allows versatile applications. In addition, although we only demonstrated two wavelengths (i.e., 266 nm and 532 nm) for *ex vivo* histological imaging and *in vivo* vasculature imaging by PAM, more wavelengths can be easily adopted for functional and metabolic PAM imaging. We believe this approach will open new prospects for high-resolution PAM applications.

Methods

Design and fabrication of DOEs

The fabrication is based on four rounds of lithography to achieve 16 heights, corresponding to a phase step of $\pi/8$, on a fused silica wafer. The phase modulation P is coupled with the structure height H via the relationship $P = 2\pi H(n' - 1)/\lambda$, where n' is the refractive index of the silica, λ is the wavelength of the incident laser. The average height interval (HI) is 33nm for 266nm laser and 72nm for 532nm laser. The first round of etching is to finish 8×HI, the second is for 4×HI, the third is for 2×HI, and the fourth is for HI. The fabrication process was completed in the Stanford Nanofabrication lab (SNF lab), and the detailed procedure is listed in Supplementary Table 2. The overall time cost of manufacturing one batch of DOEs is about 10 hours. The height accuracy during the fabrication is better than 95%, and the alignment error for the four rounds of photography is around 1 μm. Our result shows an axial intensity uniformity of ~3.6% for 200 μm×1.2 μm NB (266 nm) and ~11.1% for 1000 μm×2.3 μm NB (532 nm). The axial intensity uniformity is calculated as below:

$$\text{Uniformity} = \frac{\text{Maximal intensity} - \text{minimal intensity}}{\text{Maximal intensity} + \text{minimal intensity}}$$

Please note the maximal intensity and the minimal intensity were calculated only within the length of NB. The DOE efficiency is calculated as the ratio of the energy enclosed within the main lobe of the NB to the energy of the input Gaussian beam. To accommodate the DOE efficiency, we used a higher input pulse energy for the NB to ensure similar signal-to-noise ratios for the GB and NB at the focal plane.

NB-PAM system

The ultraviolet PAM (UV-PAM) system used an Nd: YLF (neodymium-doped yttrium lithium fluoride) Q-switched 266 nm nanosecond pulsed laser (QL266-010-O, CrystaLaser), while the visible PAM (VIS-PAM) used a 532 nm nanosecond pulsed laser (VGEN-G-20, Spectra Physics). Both the UV-PAM system and the VIS-

PAM system included a pair of plano-convex lenses for beam expansion and a high-energy pinhole for spatial filtering. The expanded and collimated laser beam was focused through a customized ring-shaped ultrasonic transducer using a custom-made water-immersion objective lens. To achieve the needle-shaped beam for an extended depth of field, we placed the customized DOE on the front surface of the objective lens. The specimen for UV-PAM was immersed in water, while the specimen and animal for VIS-PAM were placed underneath the water tank with a transparent membrane at the bottom. In UV-PAM system, a bandpass glass filter (FGUV5, Thorlabs) was used to filter out the leaked pump green light. A reconfigurable I/O device (myRIO-1900, National Instruments) was used to synchronously trigger UV laser pulses, motor scanning, and data acquisition. In the VIS-PAM, since the 532 nm laser cannot be externally triggered, a beam splitter and a photodiode (PDA36A, Thorlabs) were used to capture laser pulses and synchronize motor scanning and data acquisition. The VIS-PAM system synchronization and control were achieved by a Multifunction I/O Device (PCIe-6323, National Instruments) I/O device. Both systems included two low noise amplifiers (ZFL-500LN+, Mini-Circuits) and a 500 MHz sampling rate data acquisition card (ATS 9350, Alazar Technologies).

For system characterization, we used a positive 1951 USAF resolution target (R1DS1P, Thorlabs) to confirm the image quality and the depth-of-field. The USAF resolution target is mounted onto a 3D scanner for the raster scanning and the axial position adjustment. The pulse energy was kept below 10 nJ to avoid potential damage to the USAF resolution target. The carbon fiber phantom was prepared using 3D randomly distributed carbon fibers with a diameter of ~6 μm embedded in a 4% agarose block. The 2-12 μm diameter carbon particles (484164, MilliporeSigma) were chosen to prepare the agarose-embedded particle phantom.

UV-NB-PAM and UV-GB-PAM of fresh animal organ

Animal organs were harvested from adult Hsd: ND4 Swiss Webster mice (male, 9-10 weeks old, Envigo) and

washed using phosphate-buffered saline to remove blood on the surface. The washed fresh organs were then immersed in 2-3% low melting point agarose (A6013, MilliporeSigma) at the temperature of 37 degrees. The agarose with organ was cooled down in a 4-degree refrigerator for 10 mins to form strong gel blocks. The agarose-embedded organ block was then mounted onto the sample holder for PAM imaging. The images were acquired by 2D raster-scanning of the sample holder immersed in the water tank.

***In vivo* VIS-NB-PAM and VIS-GB PAM of mouse brain**

We used C57BL/6NHsd mice (female, 5-6 weeks old, Jackson Laboratory) for the in vivo studies. The animal was firstly anesthetized with isoflurane (~2-3% in 1.5 L/min medical grade air) in an induction chamber via a vaporizer and then transferred to a heating pad with a nosecone for surgery. During surgery, the anesthesia was maintained at 1.5% in 1 L/min medical grade air. After the mouse was anesthetized, a toe pinch procedure was conducted to confirm the anesthesia status prior to any surgical procedures. When the animal no longer reacted to the toe pinch, it was transferred to a stereotactic frame with its body temperature maintained via a heating pad. Before the surgery, the animal was given a single dose of 5 mg/kg ketoprofen. Ophthalmic ointment was applied topically to the corneal surfaces prior to surgery to prevent corneal drying. After removing the hair on the scalp, the skin was cut from the middle, and the periosteum was removed to expose the mouse brain. The mouse imaged with the skull was kept intact without thinning, while the skull was kept wet using saline and covered by ultrasound gel during PAM imaging. The mouse imaged without a skull underwent craniotomy surgery to expose the cortical vessels before imaging. A portion of the skull over the region of interest was removed using a dental drill. The drilling was paused every 30 seconds to avoid overheating the skull while the bone dust was continuously flushed by saline. After craniotomy, pre-soaked surgical sponges were applied to the exposed mouse brain to prevent further bleeding before the animal was transferred to the imaging site.

For PAM imaging, the mouse was placed onto a customized animal holder with a tooth bar and a nose cone to stabilize the brain. The mouse was maintained under anesthesia with 1.0-1.5% vaporized isoflurane in 1 L/min medical air, and the body temperature was kept at 37 °C. Ultrasound gel was applied between the water tank membrane and mouse brain to ensure ultrasound coupling. The animal holder was mounted onto a customized scanner together with the water tank. During the PAM imaging, the water tank and animal were moved together by the scanner, while the PAM detection module consisting of an ultrasonic transducer and a focusing lens was immersed in water and remained still. The mouse's respiration and body temperature were closely monitored to ensure its normal physiological conditions. The animal was euthanized by carbon dioxide after PAM imaging. All animal experiments were carried out in conformity with the protocol approved by the Institutional Animal Care and Use Committee (IACUC) of the California Institute of Technology.

Data and image processing

To reconstruct the 2D PAM maximal amplitude projection (MAP) images, we took the amplitude of the photoacoustic A-line signals after Hilbert transform for each pixel. For 3D PAM image reconstruction, deconvolution of A-line signals was implemented using the spatially invariant electrical impulse response (EIR) of the customized ultrasound transducer to improve the axial resolution. The 3D PAM images were reconstructed by the absolute value of Hilbert transformed A-line signals after the deconvolution. The axial position was determined by quantifying the maximal amplitude position in A-line signals, assuming the speed of sound is 1500 m/s in room temperature water. A median filter with a window size of 2 × 2 pixels was applied to the depth image for smooth colors. The color-encoded depth-resolved image was obtained by multiplying the 2D MAP image pixel by pixel with the depth image. To alleviate signal attenuation caused by the acoustical detection sensitivity difference along the axial direction, we performed the time-dependent gain compensation

after differentiating PA signals and system noise, ensuring uniform ultrasound detection sensitivity at different axial positions. The threshold to distinguish PA signals from noise is determined by three times the standard deviation of noises. Thus, the time-dependent gain compensation is implemented in only PA signals to avoid amplifying system noise.

Acknowledgments

L.V.W was sponsored by the United States National Institutes of Health (NIH) grants R01 EB028277, U01 NS099717 (BRAIN Initiative), and R35 CA220436 (Outstanding Investigator Award). A.d.l.Z. was supported by National Institutes of Health (NIH) grants DP50D012179 and K23CA211793, United States National Science Foundation (NSF 1438340), and United States Air Force (FA9550-15-1-0007).

Contributions

R.C. and L.V.W. designed the experiment. R.C., L.L., and Y.Z. built the photoacoustic microscopy system. J.Z. designed and fabricated diffractive optical elements. L.D. contributed to the mask preparation and wafer dividing. L.J. and Q.Z. manufactured the ultrasonic transducer. R.C. prepared the sample and animals and performed the imaging experiment. R.C., S.D., and Y.L. contributed to image processing. L.V.W and A.d.l.Z. supervised the project. All authors were involved in discussions and manuscript preparation.

Competing Interests

L.V.W. has a financial interest in MicroPhotoAcoustics, CalPACT, and Union Photoacoustic Technologies, which, however, did not support this work. The remaining authors declare no competing financial interests.

Data Availability

The authors declare that all data supporting the findings of this study are available within the paper and its Supplementary Information. The raw data are too large to be publicly shared, yet they are available for research

purposes from the corresponding authors on reasonable request.

Code Availability

The code that supports the plots and images within this paper is available from the corresponding author upon reasonable request.

Figure Legends

Figure 1. Principle of NB-PAM with a customized DOE. a DOE phase pattern for NB composed of multiple phases of M foci. **b** Principle of a DOE combining M foci to form the desired NB. **c** YZ-profile of a Gaussian beam with a focal spot size of 1.2 μm at 266 nm and XY-profile at different z positions. Scale bars, 10 μm. **d** YZ-profile of the needle-shaped beam generated by DOE for 200 μm×1.2 μm NB at 266 nm and XY-profile at different z positions. Scale bars, 10 μm. **e** Experimental setup of NB-PAM system. BS, beam sampler; PH, pinhole; CL, correction lens; UT, ultrasonic transducer; DAQ, data acquisition. **f** Principle of conventional GB-PAM. **g** Principle of NB-PAM. In **f** and **g**, simulated YZ-projection images of uniformly distributed microspheres with a diameter of 7 μm show the difference between the GB-PAM with 0.16 numerical aperture (NA) and the NB-PAM with 1000 μm×2.3 μm DOE.

Figure 2. Characterization of UV-NB-PAM in comparison with that of conventional UV-GB-PAM. a Images of a 1951 USAF resolution target at different axial positions acquired by UV-GB-PAM with 0.16 NA and UV-NB-PAM with 200 μm×1.2 μm NB. The focal plane of UV-GB-PAM is at z = 0 μm. **b, c** Close-ups of images acquired by conventional UV-GB-PAM at z = 0 μm and z = +105 μm, respectively. **d, e** Close-ups of images acquired by UV-NB-PAM at z = 0 μm and z = +105 μm, respectively. **f** Profile of element 6 from group 7 measured by conventional UV-GB-PAM and UV-NB-PAM at z = 0 μm. **g** Lateral FWHM resolutions measured by imaging a sharp edge and quantified by edge spread functions and derived line spread functions

(inset).

Figure 3. Volumetric imaging of carbon particles by UV-NB-PAM with 200 µm×1.2 µm NB and UV-GB-PAM. XY-MAP images of carbon particles acquired by **a** UV-GB-PAM and **b** UV-NB-PAM. Scale bars, 250 µm. **c** Virtually sectioned XY-MAP images at different depths by UV-GB-PAM and UV-NB-PAM after time-dependent gain compensation. Scale bars, 50 µm.

Figure 4. Depth-resolved imaging of carbon fibers by VIS-GB-PAM and VIS-NB-PAM with 1000 µm×2.3 µm NB. a VIS-GB-PAM and **b** VIS-NB-PAM of ~ 6 µm carbon fibers randomly distributed in an agarose block. Scale bar, 1 mm. The comparison of **c-f** Close-up VIS-GB-PAM images and **g-j** close-up VIS-GB-PAM images demonstrates the improved DOF Scale bars, 250 µm.

Figure 5. Label-free UV-GB-PAM and UV-NB-PAM with 200 µm×1.2 µm NB of slide-free fresh mouse lung and mouse brain. a UV-GB-PAM and **b** UV-NB-PAM of a fresh mouse lung embedded in agarose block. Scale bars, 250 µm. Close-up images of the area indicated by yellow boxes in a and b show the difference between UV-GB-PAM and UV-NB-PAM. Scale bars, 50 µm. **c** UV-GB-PAM and **d** UV-NB-PAM of a fresh mouse brain embedded in agarose block. Scale bars, 500 µm. Close-up images of representative areas in UV-GB-PAM show the compromised image quality due to out-of-focus locations. Close-up images in UV-NB-PAM show the well-maintained resolution in corresponding areas. Scale bars, 100 µm.

Figure 6. *In vivo* label-free depth-encoded VIS-NB-PAM with 1000 µm×2.3 µm NB and VIS-GB-PAM of brain vasculature with and without a skull. a VIS-GB-PAM and **b** VIS-NB-PAM of a mouse brain without a skull show the depth-encoded brain vasculature. **c** VIS-GB-PAM and **d** VIS-NB-PAM of a mouse with an intact skull show the depth-encoded brain vasculature. Both mouse brain vasculature images by VIS-NB-PAM show more blood vessels in the edge areas than the corresponding conventional VIS-GB-PAM. Scale bars, 1 mm.

References

1. Glaser, A. K. *et al.* Light-sheet microscopy for slide-free non-destructive pathology of large clinical specimens. *Nat Biomed Eng* **1**, 1–10 (2017).
2. Liu, S. & Hua, H. Extended depth-of-field microscopic imaging with a variable focus microscope objective. *Opt Express* **19**, 353–362 (2011).
3. Li, B., Qin, H., Yang, S. & Xing, D. In vivo fast variable focus photoacoustic microscopy using an electrically tunable lens. *Opt. Express, OE* **22**, 20130–20137 (2014).
4. Xiao, S., Tseng, H., Gritton, H., Han, X. & Mertz, J. Video-rate volumetric neuronal imaging using 3D targeted illumination. *Sci Rep* **8**, 7921 (2018).
5. Shain, W. J., Vickers, N. A., Goldberg, B. B., Bifano, T. & Mertz, J. Extended depth-of-field microscopy with a high-speed deformable mirror. *Opt. Lett., OL* **42**, 995–998 (2017).
6. Patel, K. B. *et al.* High-speed light-sheet microscopy for the in-situ acquisition of volumetric histological images of living tissue. *Nat. Biomed. Eng* **6**, 569–583 (2022).
7. Descloux, A. *et al.* Combined multi-plane phase retrieval and super-resolution optical fluctuation imaging for 4D cell microscopy. *Nature Photon* **12**, 165–172 (2018).
8. Geissbuehler, S. *et al.* Live-cell multiplane three-dimensional super-resolution optical fluctuation imaging. *Nat Commun* **5**, 5830 (2014).
9. Abrahamsson, S. *et al.* Fast multicolor 3D imaging using aberration-corrected multifocus microscopy. *Nat Methods* **10**, 60–63 (2013).
10. Oudjedi, L. *et al.* Astigmatic multifocus microscopy enables deep 3D super-resolved imaging. *Biomed. Opt. Express, BOE* **7**, 2163–2173 (2016).
11. Zheng, G., Horstmeyer, R. & Yang, C. Wide-field, high-resolution Fourier ptychographic microscopy. *Nature Photon* **7**, 739–745 (2013).
12. Planchon, T. A. *et al.* Rapid three-dimensional isotropic imaging of living cells using Bessel beam plane illumination. *Nat Methods* **8**, 417–423 (2011).
13. Gao, L., Shao, L., Chen, B.-C. & Betzig, E. 3D live fluorescence imaging of cellular dynamics using Bessel beam plane illumination microscopy. *Nat Protoc* **9**, 1083–1101 (2014).
14. Jia, S., Vaughan, J. C. & Zhuang, X. Isotropic three-dimensional super-resolution imaging with a self-bending point spread function. *Nature Photon* **8**, 302–306 (2014).
15. Hu, Y., Chen, Z., Xiang, L. & Xing, D. Extended depth-of-field all-optical photoacoustic microscopy with a dual non-diffracting Bessel beam. *Opt. Lett., OL* **44**, 1634–1637 (2019).
16. Yang, J., Gong, L., Shen, Y. & Wang, L. V. Synthetic Bessel light needle for extended depth-of-field microscopy. *Appl. Phys. Lett.* **113**, 181104 (2018).
17. Thériault, G., Koninck, Y. D. & McCarthy, N. Extended depth of field microscopy for rapid volumetric two-photon imaging. *Opt. Express, OE* **21**, 10095–10104 (2013).
18. Thériault, G., Cottet, M., Castonguay, A., McCarthy, N. & De Koninck, Y. Extended two-photon microscopy in live samples with Bessel beams: steadier focus, faster volume scans, and simpler stereoscopic imaging. *Frontiers in Cellular Neuroscience* **8**, (2014).
19. Snoeyink, C. Imaging performance of Bessel beam microscopy. *Opt. Lett., OL* **38**, 2550–2553 (2013).
20. Wu, Y. *et al.* Three-dimensional virtual refocusing of fluorescence microscopy images using deep learning. *Nat Methods* **16**, 1323–1331 (2019).
21. Jin, L. *et al.* Deep learning extended depth-of-field microscope for fast and slide-free histology. *Proceedings of the National Academy of Sciences* **117**, 33051–33060 (2020).

22. Zhou, Y., Sun, N. & Hu, S. Deep Learning-powered Bessel-beam Multi-parametric Photoacoustic Microscopy. 2021.12.21.473705 Preprint at https://doi.org/10.1101/2021.12.21.473705 (2021).
23. Wang, L. V. & Hu, S. Photoacoustic Tomography: In Vivo Imaging from Organelles to Organs. *Science* **335**, 1458–1462 (2012).
24. Wang, L. V. & Yao, J. A practical guide to photoacoustic tomography in the life sciences. *Nat Methods* **13**, 627–638 (2016).
25. Wong, T. T. W. *et al.* Fast label-free multilayered histology-like imaging of human breast cancer by photoacoustic microscopy. *Science Advances* **3**, e1602168.
26. Shi, J. *et al.* High-resolution, high-contrast mid-infrared imaging of fresh biological samples with ultraviolet-localized photoacoustic microscopy. *Nat. Photonics* **13**, 609–615 (2019).
27. Wong, T. T. W. *et al.* Label-free automated three-dimensional imaging of whole organs by microtomy-assisted photoacoustic microscopy. *Nat Commun* **8**, 1386 (2017).
28. Zhang, C., Zhang, Y. S., Yao, D.-K., Xia, Y. & Wang, L. V. Label-free photoacoustic microscopy of cytochromes. *J Biomed Opt* **18**, 020504 (2013).
29. Yao, J. *et al.* High-speed label-free functional photoacoustic microscopy of mouse brain in action. *Nat Methods* **12**, 407–410 (2015).
30. Cao, R. *et al.* Functional and oxygen-metabolic photoacoustic microscopy of the awake mouse brain. *NeuroImage* **150**, 77–87 (2017).
31. Cao, R. *et al.* Photoacoustic microscopy reveals the hemodynamic basis of sphingosine 1-phosphate-induced neuroprotection against ischemic stroke. *Theranostics* **8**, 6111–6120 (2018).
32. Zhou, Y., Xing, W., Maslov, K. I., Cornelius, L. A. & Wang, L. V. Handheld photoacoustic microscopy to detect melanoma depth in vivo. *Opt Lett* **39**, 4731–4734 (2014).
33. He, Y. *et al.* Label-free imaging of lipid-rich biological tissues by mid-infrared photoacoustic microscopy. *JBO* **25**, 106506 (2020).
34. Buma, T., Conley, N. C. & Choi, S. W. Multispectral photoacoustic microscopy of lipids using a pulsed supercontinuum laser. *Biomed Opt Express* **9**, 276–288 (2017).
35. Maslov, K., Zhang, H. F., Hu, S. & Wang, L. V. Optical-resolution photoacoustic microscopy for *in vivo* imaging of single capillaries. *Opt. Lett., OL* **33**, 929–931 (2008).
36. Hu, S., Maslov, K. & Wang, L. V. Second-generation optical-resolution photoacoustic microscopy with improved sensitivity and speed. *Opt. Lett., OL* **36**, 1134–1136 (2011).
37. Park, B. *et al.* Reflection-mode switchable subwavelength Bessel-beam and Gaussian-beam photoacoustic microscopy in vivo. *Journal of Biophotonics* **12**, e201800215 (2019).
38. Jiang, B., Yang, X. & Luo, Q. Reflection-mode Bessel-beam photoacoustic microscopy for in vivo imaging of cerebral capillaries. *Opt. Express, OE* **24**, 20167–20176 (2016).
39. Shi, J., Wang, L., Noordam, C. & Wang, L. V. Bessel-beam Grueneisen relaxation photoacoustic microscopy with extended depth of field. *J Biomed Opt* **20**, 116002 (2015).
40. Zhou, Y., Sun, N. & Hu, S. Deep Learning-powered Bessel-beam Multi-parametric Photoacoustic Microscopy. *IEEE Trans Med Imaging* **PP**, (2022).
41. Xu, Z. *et al.* Cortex-wide multiparametric photoacoustic microscopy based on real-time contour scanning. *NPh* **6**, 035012 (2019).
42. Ning, B. *et al.* Ultrasound-aided Multi-parametric Photoacoustic Microscopy of the Mouse Brain. *Sci Rep* **5**, 18775 (2015).
43. Yang, X., Jiang, B., Song, X., Wei, J. & Luo, Q. Fast axial-scanning photoacoustic microscopy using tunable acoustic gradient lens. *Opt. Express, OE* **25**, 7349–7357 (2017).

44. Liu, S. *et al.* GPU-accelerated two dimensional synthetic aperture focusing for photoacoustic microscopy. *APL Photonics* **3**, 026101 (2018).
45. Jeon, S., Park, J., Managuli, R. & Kim, C. A Novel 2-D Synthetic Aperture Focusing Technique for Acoustic-Resolution Photoacoustic Microscopy. *IEEE Transactions on Medical Imaging* **38**, 250–260 (2019).
46. Amjadian, M., Mostafavi, S. M., Chen, J., Wang, L. & Luo, Z. Super-Resolution Photoacoustic Microscopy via Modified Phase Compounding. *IEEE Trans Med Imaging* **PP**, (2022).
47. Amjadian, M. *et al.* Super-Resolution Photoacoustic Microscopy Using Structured-Illumination. *IEEE Transactions on Medical Imaging* **40**, 2197–2207 (2021).
48. Yang, J. *et al.* Motionless volumetric photoacoustic microscopy with spatially invariant resolution. *Nat Commun* **8**, 780 (2017).

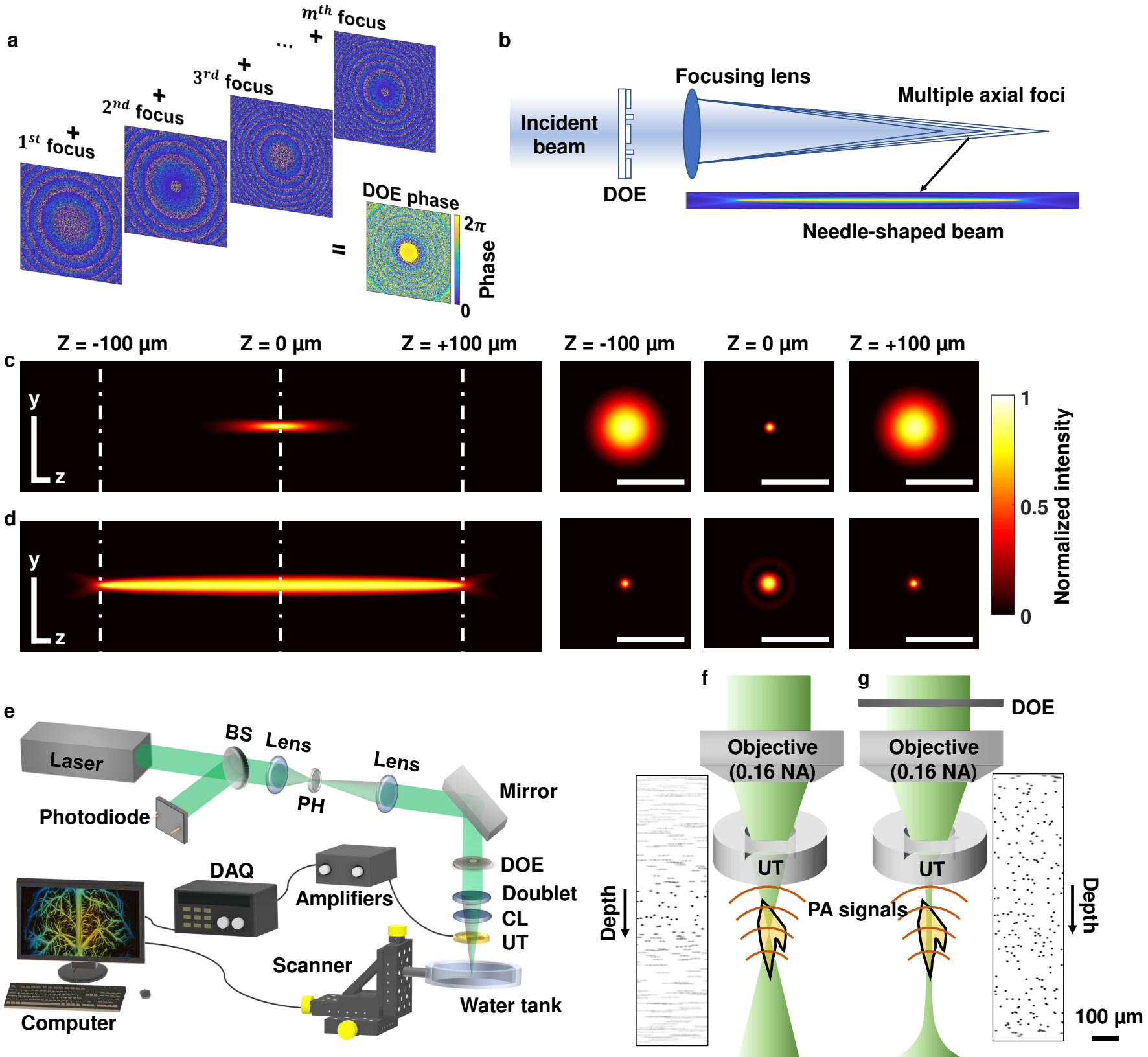
a
1^{st} focus
2^{nd} focus
3^{rd} focus
...
m^{th} focus
DOE phase
2π
Phase
0
b
Incident beam
DOE
Focusing lens
Multiple axial foci
Needle-shaped beam
c
d
Z = -100 μm
Z = 0 μm
Z = +100 μm
Z = -100 μm
Z = 0 μm
Z = +100 μm
y
z
1
0.5
0
Normalized intensity
e
Laser
BS
Lens
PH
Lens
Mirror
Photodiode
DAQ
Amplifiers
DOE
Doublet
CL
UT
Scanner
Water tank
Computer
f
g
Objective (0.16 NA)
Objective (0.16 NA)
DOE
UT
UT
PA signals
Depth
Depth
100 μm

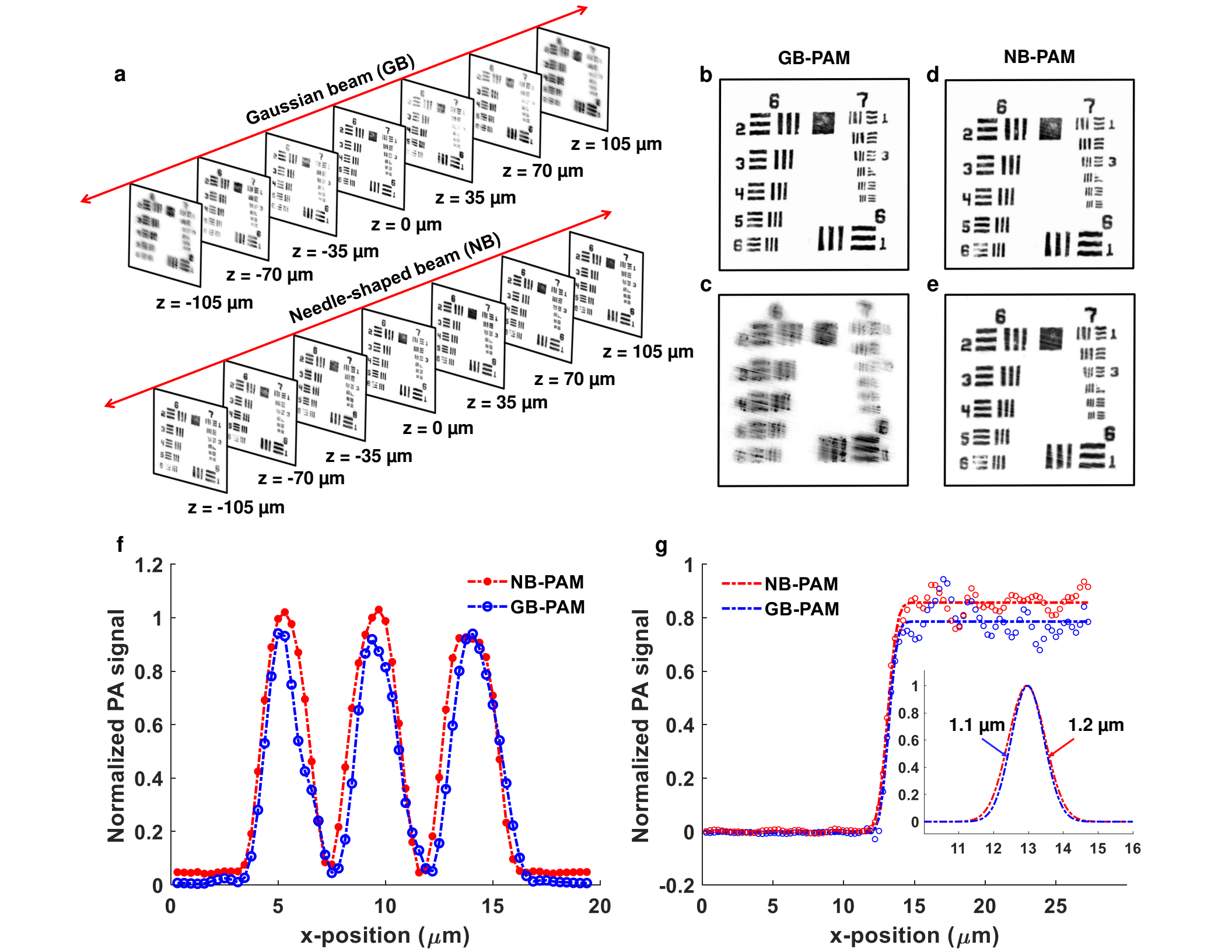
a
Gaussian beam (GB)
z = -105 µm
z = -70 µm
z = -35 µm
z = 0 µm
z = 35 µm
z = 70 µm
z = 105 µm
Needle-shaped beam (NB)
z = -105 µm
z = -70 µm
z = -35 µm
z = 0 µm
z = 35 µm
z = 70 µm
z = 105 µm
b
GB-PAM
d
NB-PAM
c
e
f
NB-PAM
GB-PAM
Normalized PA signal
x-position (µm)
g
NB-PAM
GB-PAM
Normalized PA signal
x-position (µm)
1.1 µm
1.2 µm

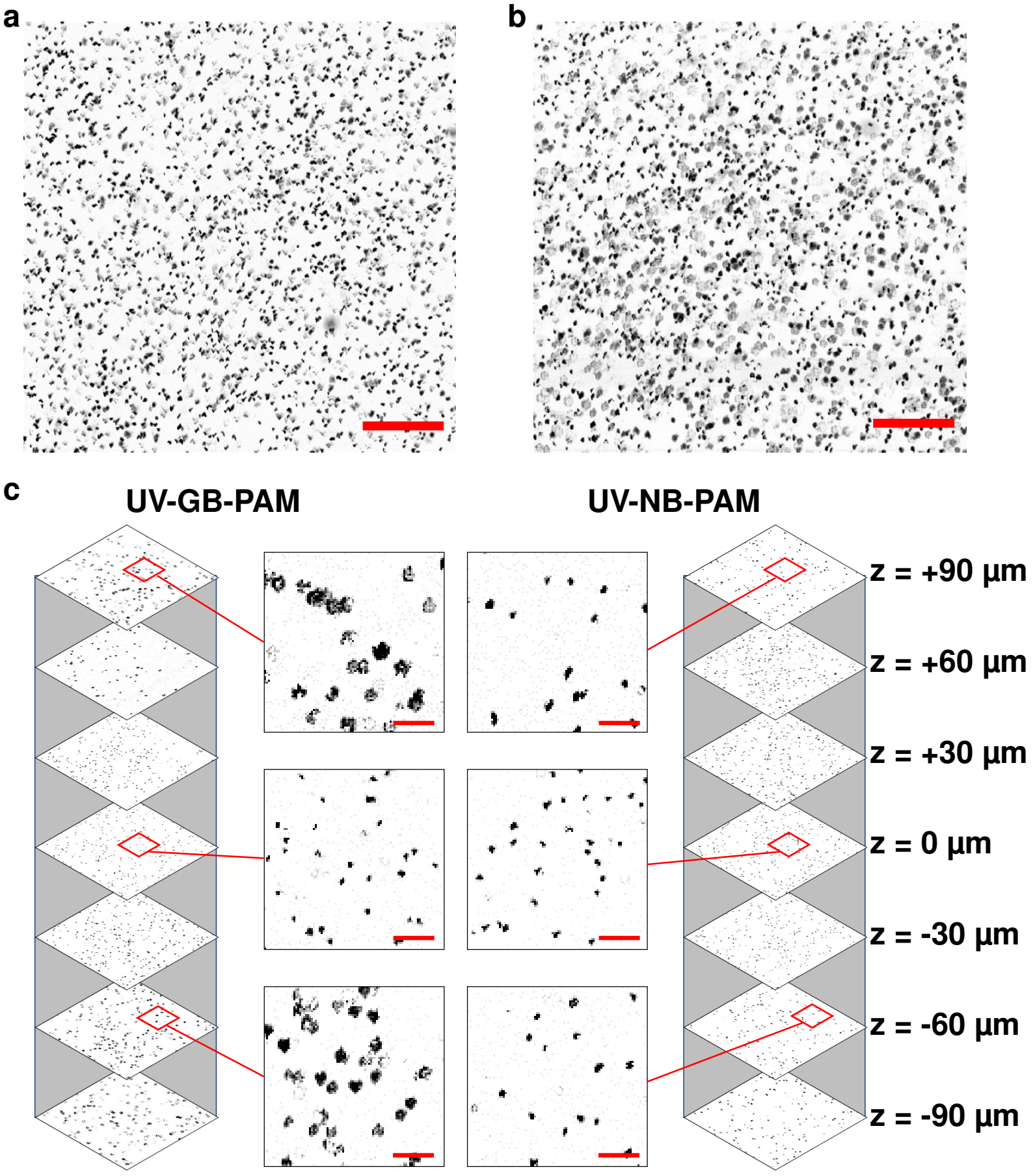
a
b
c
UV-GB-PAM
UV-NB-PAM
z = +90 μm
z = +60 μm
z = +30 μm
z = 0 μm
z = -30 μm
z = -60 μm
z = -90 μm

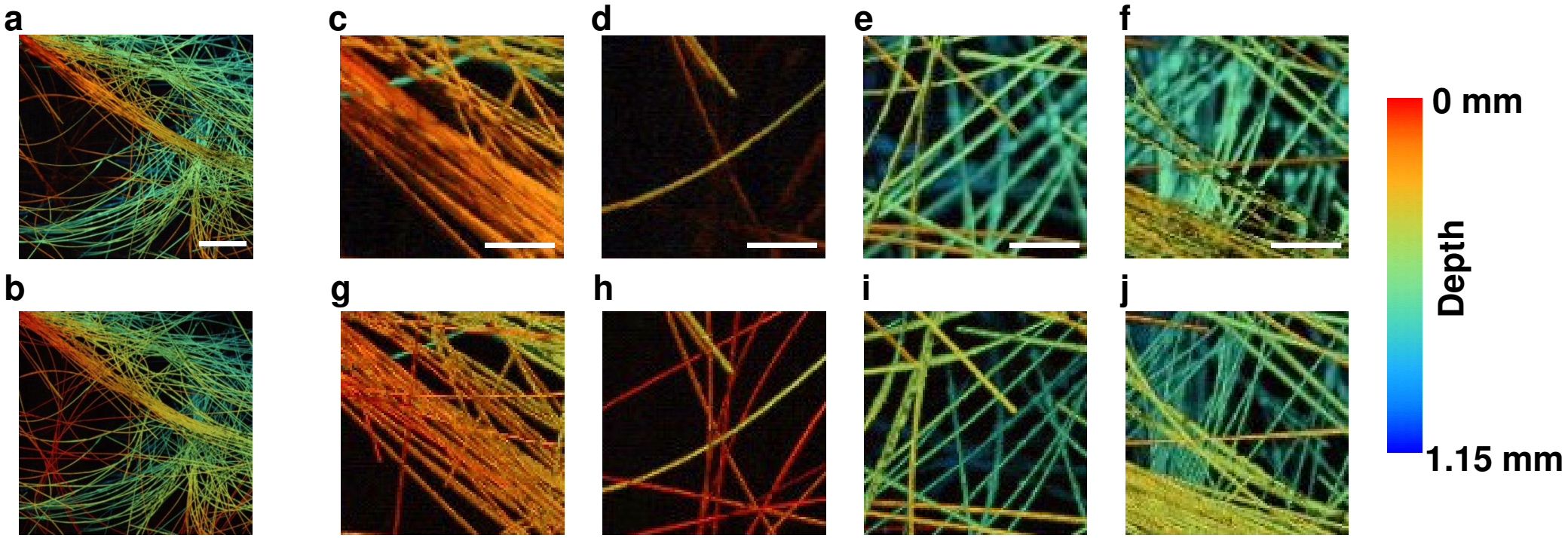
a
c
d
e
f
b
g
h
i
j
0 mm
Depth
1.15 mm

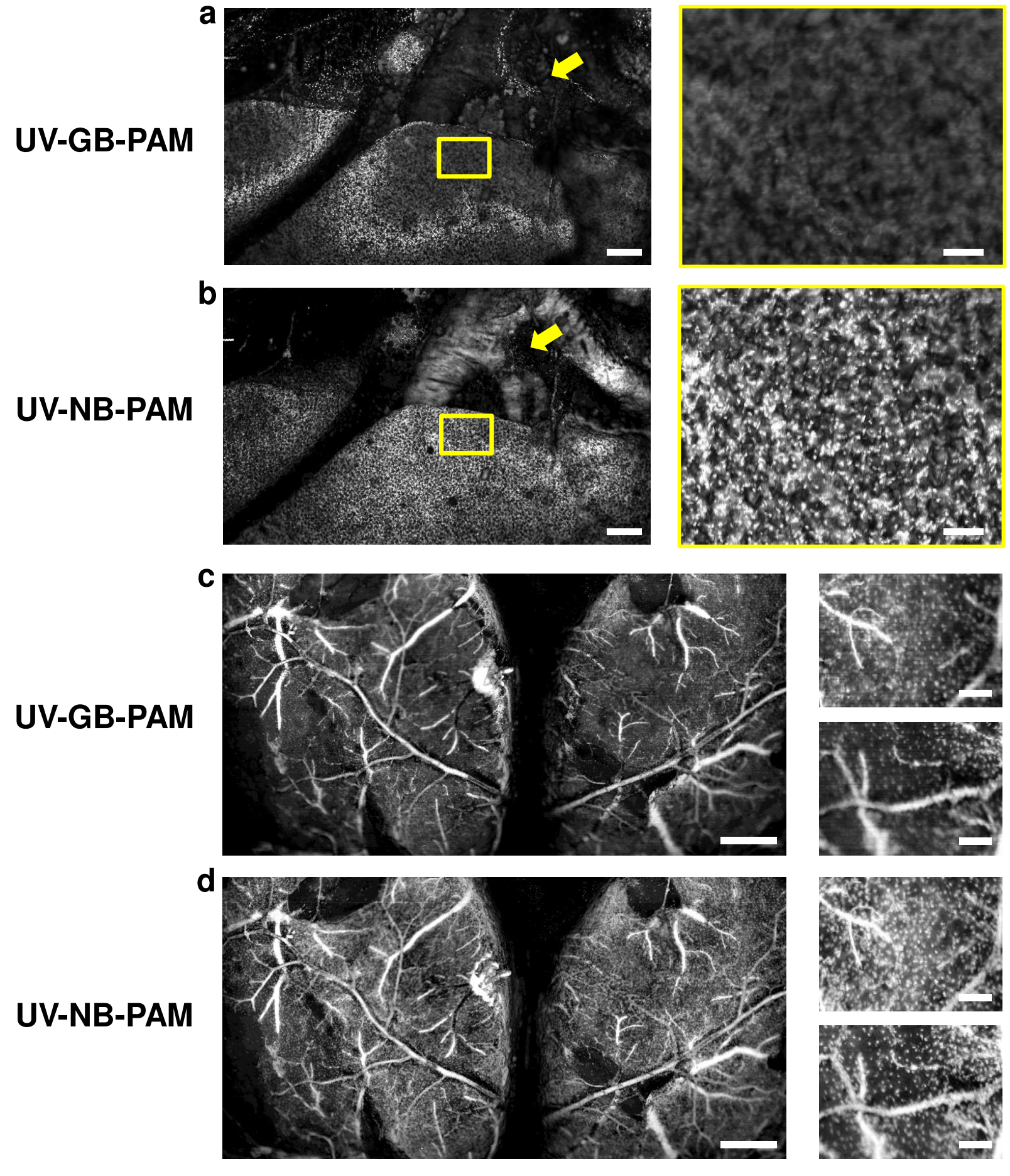
a
UV-GB-PAM
b
UV-NB-PAM
c
UV-GB-PAM
d
UV-NB-PAM

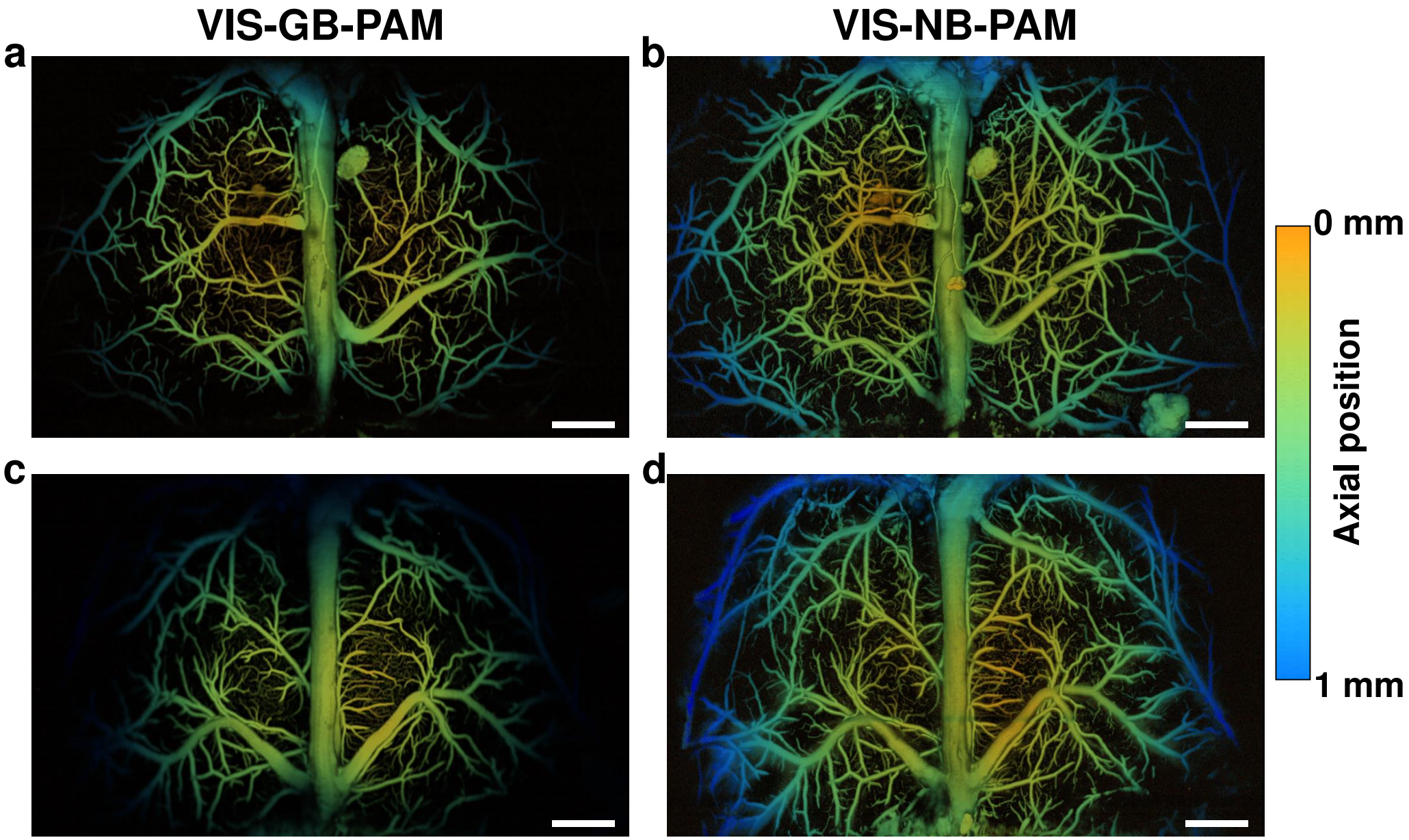
VIS-GB-PAM
VIS-NB-PAM
a
b
c
d
0 mm
Axial position
1 mm